J. of Supercritical Fluids 84 (2013) 61–73

Contents lists available at ScienceDirect

The Journal of Supercritical Fluids

journal homepage: www.elsevier.com/locate/supflu

Large-eddy simulation of supercritical fluid injection

X. Petit, G. Ribert*, G. Lartigue, P. Domingo

CORIA - CNRS, Normandie Université, INSA de Rouen, Technopôle du Madrillet, BP 8, 76801 Saint-Etienne-du-Rouvray, France

ARTICLE INFO

Article history:
Received 7 June 2013
Received in revised form
24 September 2013
Accepted 25 September 2013

Keywords:
Supercritical
LES
Mixing
3D-NSCBC

ABSTRACT

Mixing is a key point for thrust and efficiency of combustion systems. It becomes crucial in the case Liquid Rocket Engines as large investments are involved. Besides, the pressure in liquid rocket combustion chamber often exceeding the critical point of loaded propellants, mixing becomes an important scientific issue as fluid properties differ from classical ideal gas assumption. In this study, two configurations are studied to evaluate the impact of subgrid models on mixing. Firstly, Mayer's experiments of trans- and supercritical nitrogen jet injection into a warm nitrogen atmosphere have been numerically investigated with a structured numerical code called SiTCom-B. SiTCom-B solves Direct Numerical Simulations and Large Eddy Simulations equations for perfect or real gas equation of states. In this study, Soave–Redlich–Kwong (SRK) and Peng–Robinson equation of state are used with appropriated thermodynamics relations and validated against NIST data. Three-dimensional LES are conducted for two cases (cases 3 and 4 in Mayer et al.'s reference [1]) with real-gas NSCBC treatment. Several sub-grid scale models are tested and the results are compared to experimental data for density on jet axis: a very good agreement is obtained on a light mesh (11.6 million of points) with the SRK equation of state and standard Smagorinsky model. Flow structures are evidenced with Schlieren snapshots. Secondly, the Mascotte test-bench from ONERA is simulated with SiTCom-B based on Soave–Redlich–Kwong equation of state and Smagorinsky models. The simulated non-reacting case is characterized by a very short liquid oxygen dense core because of the strong density and velocity gradients boosting mixing efficiency.

© 2013 Elsevier B.V. All rights reserved.

1. Introduction

Many combustion devices involve thermodynamic phase transition from a subcritical to a supercritical state. As example, the high-pressure combustion chambers of rocket engines operate in pressure and temperature range well above the thermodynamic critical points of the injected propellants (typically H_2 and O_2), *i.e.* in a *supercritical* state; the pressure is of the order of 10.0 MPa to be compared to the critical pressure of propellants, *e.g.* 1.3 MPa for hydrogen and 5.0 MPa for oxygen. Another example are the jet engines of aircraft. In order to increase the efficiency and thus reduce the CO_2 emissions, a general trend toward the increase pressure in the combustion chamber can be observed as well as the development of special designs of combustion chambers (LPP: Lean-Premix-Prevaporized or RQL: Rich-Quench-Lean) to limit NO_x production. As a consequence, the liquid fuel may be injected in an environment, whose conditions are above the critical properties of the fuel. Generally, the chamber pressure is above the critical pressure of the fuel ($p > p_c$) but the injection temperature is subcritical ($T < T_c$). For example, the critical properties of decane which is commonly used to simulate kerosene, are $p_c = 2.1$ MPa and $T_c = 617.7$ K. Such a state is called *compressed fluids* (or *transcritical* state [2]). After injection, the fuel heats up and its temperature exceeds its critical value ($T > T_c$). In the two cases the fluid is neither a liquid nor a gas, but may have liquid-like density with gas-like properties; beyond the critical point (p_c, T_c), there is no distinction between gaseous and liquid phases. Around the critical point or the pseudo-boiling line, large variations of these transport or thermodynamics properties are observed and lead to strong gradients. Finally, a similar issue is observed for car engines with recent diesel injection devices as shown by Oefelein and Lacaze [3].

Studies on supercritical fluid flows have been mainly driven by research on space propulsion, where understanding the complex environment of a rocket engine combustion chamber is a tough challenge. The present study is focused on injection under supercritical conditions that may drive the efficiency of mixing, combustion or heat transfer. Much experimental work has already been accomplished for sub- and super-critical cold jets [1,4–9]. All these studies show a striking difference between the disintegration of these two types of jet: in subcritical regime, jets break into several drops and liquid ligaments, following the classical atomization process, while in supercritical regime, ligaments and droplets, are replaced by thread form elements, *i.e.* finger-like structures, emerging from the jet core, and located in areas farthest from the injector. These structures are dense fluid portion detaching from

* Corresponding author: Tel.: +33 232959792.
E-mail addresses: guillaume.ribert@coria.fr, guillaume.ribert@insa-rouen.fr (G. Ribert).

0896-8446/$ – see front matter © 2013 Elsevier B.V. All rights reserved.
http://dx.doi.org/10.1016/j.supflu.2013.09.011

EoS	equation of state
FOC	first order correction
HWHM	half width, half maximum
MILES	monotone integrated LES
PR	Peng–Robinson
RK	Redlich–Kwong
SCS	scale-similarity
SGS	sub-grid scale
SM	Smagorinsky
SMD	dynamic Smagorinsky
SRK	Soave–Redlich–Kwong
VDW	Van der Waals
VR	Vreman
WL	WALE

the jet before quickly dissolving in the surrounding atmosphere. Typically, supercritical jets look like gas jets with liquid jet densities. These studies also show a reduction of turbulence compared to classical atmospheric jets because of the strong density gradients encountered into the flow. However, very few experimental data are available especially for realistic rocket engines conditions because of the hostile environment inside the chamber. For example, Conley et al. [10] recently provided quantitative data for the heat flux along the outer wall of the chamber.

Along with these experimental investigations, several theoretical and numerical efforts have been made in order to analyze and study specific phenomena of supercritical regime. These studies are relatively recent and turbulence modeling for Reynolds Average Navier–Stokes (RANS) or Large Eddy Simulation (LES) tools is still required [11]. In this context, LES of supercritical mixing and injection [12–15] have often been realized with classical models (Smagorinsky [16], WALE [17]) and a stabilizing effect of the density gradient with a turbulent energy redistribution along the mixing layer was identified. Similar results were observed through the direct numerical simulations (DNS) performed by Miller et al. [18,19], Bellan and O'Kongo [20,21] or Oefelein [22].

To simulate supercritical fluids, the classical compressible Navier–Stokes equations for a perfect gas have to be modified as follow: an equation of state (EoS) that accounts for real-gas effects must be implemented and thermodynamics as well as transport models must be pressure-dependent [23].

The next section is dedicated to the numerical solver presentation. Special attention is drawn on thermodynamics which plays a major role in this study and also on boundary conditions for compressible real gases. The effects of both state equation and sub grid modeling on the results are analyzed. In Section 3, two configurations are under study: Mayer et al.'s experiment [1] that is a trans- or super-critical nitrogen injection into warm nitrogen and a methane/liquid oxygen (LO_x) co-axial injector representative of future rocket engines. 3D simulations are performed for both cases and comparisons are realized with the available experimental data.

2. Thermodynamics and numerical solver

Simulations are realized with an home-made code called "SiTCom-B" (Simulation of Turbulent Combustion with Billions of points). SiTCom-B is a finite volume code that solves the unsteady compressible reacting Navier–Stokes equations on cartesian meshes. This new version of SiTCom [24–27] is designed to perform DNS and highly resolved LES on thousands of processors[1].

[1] http://www.coria-cfd.fr/index.php/SiTCom-B.

Table 1
Cubic EoS coefficients.

EoS	u	w	$b \times p_c/(\mathcal{R}T_c)$	$a \times p_c/(\mathcal{R}^2T_c^2)$	$\alpha(T,\omega)$
VDW	0	0	0.125	0.421875	1
RK	1	0	0.08664	0.42748	$\frac{1}{T^{0.5}}$
SRK	1	0	0.08664	0.42748	$f_{SRK}(\omega, T_c)$
PR	2	−1	0.07780	0.42748	$f_{PR}(\omega, T_c)$
SRK-PR	$\delta_1+\delta_2$	$\delta_1\delta_2$	$\frac{1}{3y+d-1}$	$\frac{3y^2+3yd+d^2+d-1}{(3y+d-1)^2}$	$\left(\frac{3}{2+T/T_c}\right)^k$

2.1. Thermodynamic

To simulate supercritical flows, SiTComb-B numerical code features real gas thermodynamic [28]: a cubic EoS replaces the classical ideal gas law, linking the pressure, p, temperature, T and density, ρ, as

$$p = \frac{\rho\mathcal{R}T}{W-b\rho} - \frac{\rho^2 a\alpha(T,\omega)}{W^2+ubW\rho+wb^2\rho^2}, \tag{1}$$

where $\mathcal{R}$ is the universal gas constant and W the molecular weight of the fluid mixture. u and w in Eq. (1) are chosen according to the desired model of EoS: Van der Waals (VDW), Redlich–Kwong (RK), Soave–Redlich–Kwong (SRK) or Peng–Robinson (PR) [23]. These EoS include attractive forces among particles, a, co-volume of particles, b, and acentric factor, ω, this latter quantifying the deviation from the spherical symmetry in a molecule. α is a function depending on T and ω. These parameters are calculated with the Van der Waals mixing rules:

$$\begin{aligned} a\alpha &= \sum_{i=1}^{N_s}\sum_{j=1}^{N_s} X_iX_j\alpha_{ij}a_{ij}, \quad \alpha_{ij}a_{ij} = \sqrt{\alpha_i\alpha_j a_i a_j}(1-\kappa_{ij}) \\ \text{and} \quad b &= \sum_{i=1}^{N_s} X_i b_i. \end{aligned} \tag{2}$$

X_k is the mole fraction of species k (among N_s species) and κ_{ij} the binary interaction coefficient. The constants a_i, b_i and α_i are determined from universal relationships [29,30], involving the critical temperature and partial pressure of species k, T_{c_k} and p_{c_k}, respectively, as well as the acentric factor ω_k. Oefelein [22] recommends to use the PR EoS for simulations with strong heat release, but SRK EoS is much more precise for low temperatures. More recently, Cismondi and Mollerup [31] developed a three-parameter SRK-PR EoS combining the advantages of the two SRK and PR EoS. Eq. (1) is then replaced by

$$p = \frac{\rho\mathcal{R}T}{W-b\rho} - \frac{\rho^2 a\alpha(T,\omega)}{(W+\delta_1 b\rho)(W+\delta_2 b\rho)}, \tag{3}$$

with $\delta_2 = \frac{1-\delta_1}{1+\delta_1}$ and $\delta_1 = d_1 + d_2(d_3 - 1.168Z_c)^{d_4} + d_5(d_3 - 1.168Z_c)^{d_6}$. d_i, for $i \in [1,6]$, are model constants given by Cismondi and Mollerup [31]; Z_c is the critical compressibility factor of fluid. Note that if $\delta_1 = 1$ or $\delta_1 = 1+\sqrt{2}$, SRK and PR EoS are recovered, respectively. Parameters used in our simulations are summarized in Table 1, but complementary derivations may be found in the articles of Meng and Yang [30] or Kim et al. [32].

In Table 1, $d = (1+\delta_1^2)/(1+\delta_1)$ and $y = 1 + [2(1+\delta_1)]^{1/3} + [4/(1+\delta_1)]^{1/3}$. k and f are functions of ω and T_c (see Cismondi and Mollerup [31]). Thermodynamic properties such as the heat capacity at constant pressure are derived using departure functions as done in Meng and Yang [30].

Classical techniques used to evaluate transport properties (viscosity, μ, and thermal conductivity, λ) are replaced by accurate high-pressure relations proposed by Chung et al. [33], which extends the Chapman–Enskog theory by introducing a dense-fluid correction. The binary mass diffusivity are predicted by the

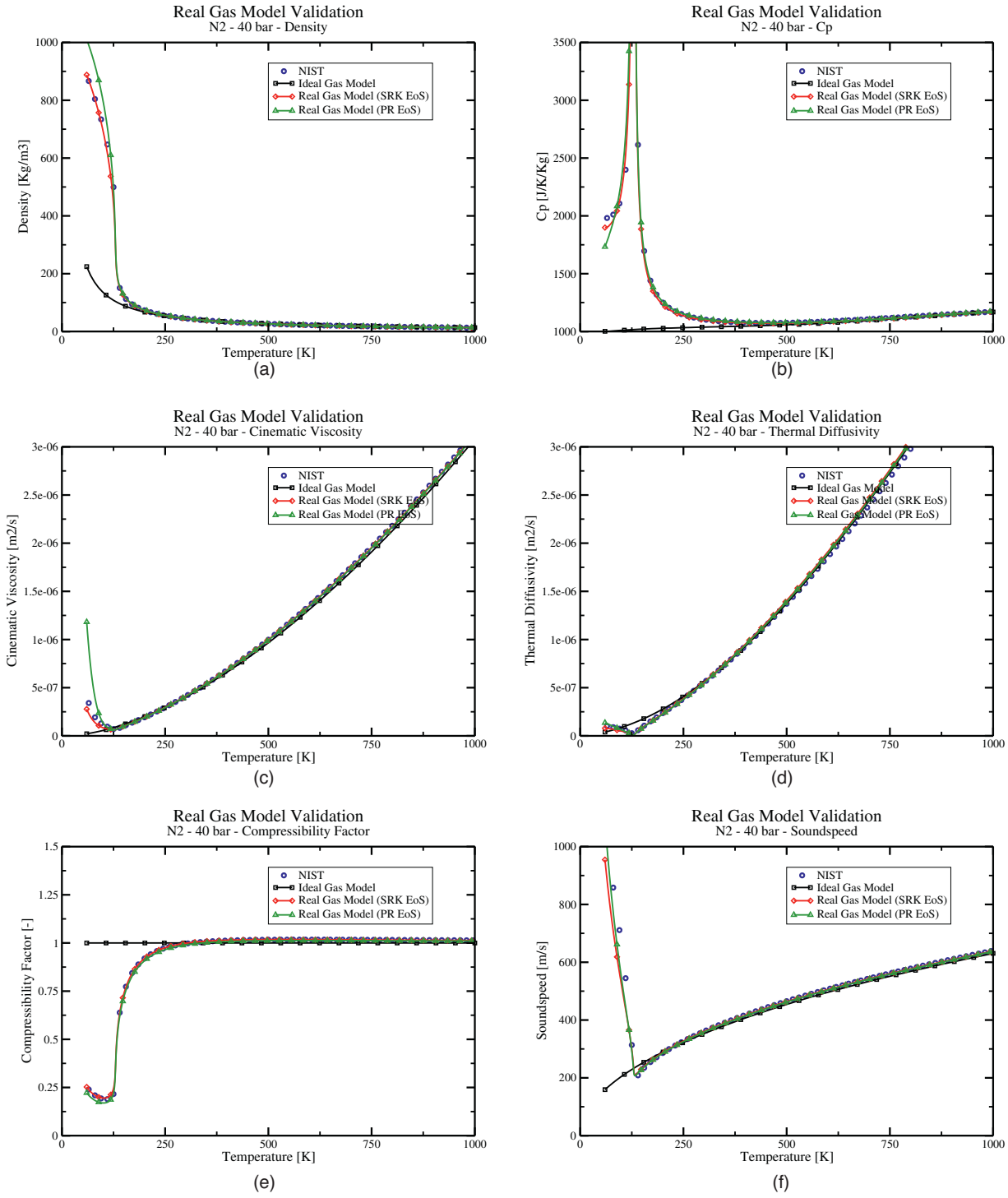

Fig. 1. Real gas thermodynamics based on SRK and PR EoS. PG and RG stand for perfect and real gas, respectively.

Takahashi method [34]. Fig. 1 shows the validation of thermodynamic for nitrogen species ($p_c = 3.34$ MPa, $T_c = 126.2$ K) at a pressure of 4 MPa. Comparisons with National Institute of Standards and Technology (NIST[2]) data are found in good agreement for density, heat capacity at constant pressure, compressibility, cinematic viscosity or thermal diffusivity. More precisely, the pseudo-boiling line that represents the prolongation of the gas/liquid phase-change line and corresponds to a maximum of constant-pressure heat capacity for a given pressure, is well recovered with the SRK or PR EoS using either the formalism of Eqs. (1) or (3). This line corresponds to the change of slope in Figs. 1. Above a temperature of 250 K, nitrogen behaves as a gas-like fluid since the compressibility factor $Z = pW/(\rho\mathcal{R}T)$ approximates the unity. However, when the temperature decreases below 250 K, the response of the heat capacity at constant pressure (C_p) for real gas (Fig. 1(b)) becomes non-linear and Z moves away from unity. Until the temperature decreases to around 130 K, departures of nitrogen characteristics from ideal gas calculations stay moderate, except

[2] http://webbook.nist.gov.

for C_p. However, below 130 K, these characteristics quickly vary to reach liquid-like values. In this last part, SRK and PR EoS exhibits small discrepancies, the SRK EoS matching very well with NIST data.

2.2. Governing equations

SiTCom-B numerical code solves the fully coupled conservation equations of species, momentum and energy. In a LES context, a Favre filtering operator is applied to the instantaneous conservation equations. If N_s is the number of species, u_i the velocity component in the x_i-axis (spatial coordinate) and t the time, then LES equations for supercritical flows may be written [11] as:

- Species mass fractions (Y_k):

$$\frac{\partial(\bar{\rho}\tilde{Y}_k)}{\partial t} + \frac{\partial(\bar{\rho}\tilde{Y}_k\tilde{u}_i)}{\partial x_i} = -\frac{\partial \bar{\rho}F^d_{k,i}}{\partial x_i} - \frac{\partial \bar{\rho}F^c_{k,i}}{\partial x_i} \quad k = 1, \ldots, N_s \tag{4}$$

The species-mass flux is expressed using the Hirschfelder and Curtiss approximation based on filtered quantities:

$$F^d_{k,i} = D_k \frac{W_k}{W}\frac{\partial \tilde{X}_k}{\partial x_i},$$

with X_k the species molar fraction. W_k is the atomic weight of species k and D_k is the diffusion coefficient of species k in the mixture. The sub-grid scale (SGS) flux $F^c_{k,i} = (\tilde{Y}_k\tilde{u}_i - \widetilde{Y_k u_i})$ requires a model.

- Momentum:

$$\frac{\partial(\bar{\rho}\tilde{u}_i)}{\partial t} + \frac{\partial(\bar{\rho}\tilde{u}_i\tilde{u}_j)}{\partial x_j} = -\frac{\partial \bar{p}}{\partial x_i} + \frac{\partial \sigma_{ij}}{\partial x_j} + \frac{\partial \tau_{ij}}{\partial x_j} \tag{5}$$

where the viscous stress tensor, σ_{ij}, and pressure, p, are expressed based on Newtonian fluids (Eq. (6)) and cubic EoS (Eqs. (1) or (3)), respectively, both of them depending on the filtered quantities.

$$\sigma_{ij} = \mu(\tilde{T}, \widetilde{Y}_k, \bar{p})\left[\left(\frac{\partial \tilde{u}_i}{\partial x_j} + \frac{\partial \tilde{u}_j}{\partial x_i}\right) - \frac{2}{3}\frac{\partial \tilde{u}_k}{\partial x_k}\delta_{ij}\right]. \tag{6}$$

$\bar{p}$ and $\tau_{ij} = \bar{\rho}(\tilde{u}_i\tilde{u}_j - \widetilde{u_i u_j})$ also require a model to close the system of equations.

- Total non chemical energy (E):

$$\frac{\partial(\bar{\rho}\tilde{E})}{\partial t} + \frac{\partial(\bar{\rho}\tilde{E}\tilde{u}_i)}{\partial x_i} = -\frac{\partial \bar{p}\tilde{u}_i}{\partial x_i} - \frac{\partial q_i}{\partial x_i} + \frac{\partial \sigma_{ij}\tilde{u}_i}{\partial x_j} + \frac{\partial \bar{\rho}\mathcal{H}_i}{\partial x_i} \tag{7}$$

where

$$q_i = -\lambda(\tilde{T}, \widetilde{Y}_k, \bar{p})\frac{\partial \tilde{T}}{\partial x_i} + \bar{\rho}\sum_{k=1}^{N_s} h_k F^d_{k,i},$$

with h_k the enthalpy of species k. $\mathcal{H}_i$ is a flux of energy depending on enthalpy h as, $\mathcal{H}_i = (\tilde{h}\tilde{u}_i - \widetilde{hu_i}) + (p\tilde{u}_i - \bar{p}\tilde{u}_i)$, and requires a model.

Unknown SGS fluxes ($F^c_{k,i}$, τ_{ij} and $\mathcal{H}_i$) have been expressed using either the constant [16] or dynamic [35] Smagorinsky closures (acronym SM and SMD, respectively), WALE (WL) [17] or Vreman (VR) [36] models. In Eq. (5), the pressure term is modeled using the filtered field: $\overline{p(\phi)} = p(\bar{\phi})$ with $\phi = \{\rho u_i, \rho E, \rho Y_k\}$.

Finally, the inlet velocity distribution, u_i, is prescribed by

$$\frac{u_1}{u_{max}} = \left(\frac{R-r}{R}\right)^{1/n} \times (1 + u_{1,turb}),$$

$$\frac{u_i}{u_{max}} = \left(\frac{R-r}{R}\right)^{1/n} \times u_{i,turb} \text{for} \quad i = 2, 3,$$

where $u_{i,turb}$ are extracted from an homogenous isotropic turbulence (HIT) with a specified intensity of turbulence (0 or 5% in the present case). R is the injection pipe radius and coefficient $n = 7$. The maximum velocity, u_{max} is given by

$$\frac{u_b}{u_{max}} = \frac{2n^2}{(n+1)\times(2n+1)}, \tag{8}$$

with u_b the bulk velocity. HIT flow fields are prescribed by a Passot–Pouquet spectrum.

2.3. Numerics

In this study, a 4th skew-symmetric-like scheme [37] for the spatial integration, and a 4th order Runge-Kutta method for the time integration are used to solve the fully coupled set of equations (Eqs. (4–24)). In order to avoid spurious numerical oscillations inherent to the presence of strong density gradients and the use of high order central scheme for the spatial integration, 2nd ($\epsilon^{[2]}$) and 4th ($\epsilon^{[4]}$) order numerical dissipation [38,39] are used to stabilize the simulations:

$$\epsilon^{[2]} = \min(\alpha_1, \alpha_2\Psi) \quad \text{and} \quad \epsilon^{[4]} = \max(0, \beta_1 - \beta_2\epsilon^{[2]}), \tag{9}$$

where users' parameters are set to $\alpha_1 = 0.5$, $\alpha_2 = 0.5$, $\beta_1 = 0.3$ and $\beta_2 = 1.0$ in this study. Ψ is a sensor based on density and pressure variables defined as follow:

$$\Psi = \frac{\Psi^{p^2} + \Psi^{\rho^2}}{\Psi^p + \Psi^\rho + \epsilon_0}, \tag{10}$$

with

$$\Psi_i^\phi = \frac{|\phi_{i+1} - 2\phi_i + \phi_{i-1}|}{(1-\omega_\Psi)\Phi_{TVD} + \omega_\Psi\Phi_{JST} + \epsilon_0}, \quad \text{with} \quad \phi = \{\rho, p\}. \tag{11}$$

The subscript $_i$ is the cell number and ϵ_0 is a threshold to ensure that the denominator cannot be zero. The value of ω_Ψ is typically 0.5. In Eq. (11),

$$\Phi_{TVD} = |\phi_{i+1} - \phi_i| + |\phi_i - \phi_{i-1}| \quad \text{and} \quad \Phi_{JST} = \phi_{i+1} + 2\phi_i + \phi_{i-1}. \tag{12}$$

This procedure ensures that the artificial viscosity is applied only to zones of interest, *i.e.* where either strong gradients of density or pressure variables are detected.

2.4. Boundary conditions

For compressible numerical codes, boundary conditions must be accurately handled [27,40,41]. Extending the work of Lodato et al. [27] to a multi-species formulation featuring real gas effects, *i.e.* with the use of $\{u_n, u_{s_1}, u_{s_2}, p, \rho_k\}$ as set of primitive variables ($\rho_k = \rho Y_k$), Euler equations are written at the face boundary as follow:

$$\frac{\partial u_n}{\partial t} = -\frac{c}{2}\left(\tilde{L}^+ - \tilde{L}^-\right) \tag{13}$$

$$\frac{\partial u_{s_1}}{\partial t} = -c\tilde{L}^{s_1} \tag{14}$$

$$\frac{\partial u_{s_2}}{\partial t} = -c\tilde{L}^{s_2} \tag{15}$$

$$\frac{\partial p}{\partial t} = -\frac{\rho c}{2}\left(\tilde{L}^+ + \tilde{L}^-\right) \tag{16}$$

$$\frac{\partial \rho_k}{\partial t} = \rho\tilde{L}^{s_k} - \frac{\rho_k}{2}\left(\tilde{L}^+ + \tilde{L}^-\right) \tag{17}$$

The non-dimensional wave strengths $\tilde{L}^*$ are a combination of the wave strengths in the local basis $(\mathcal{B})$: $\tilde{L}^* = \tilde{L}^*_n + \tilde{L}^*_{s_1} + \tilde{L}^*_{s_2}$. n is the unit vector normal to the boundary surface, pointing in the outward direction and the two other vectors s_1 and s_2 are chosen so that $\mathcal{B}$ is a direct orthonormal basis. They are given by:

$$\tilde{L}^*_n = \begin{bmatrix} \tilde{L}^+_n \\ \tilde{L}^-_n \\ \tilde{L}^{s_1}_n \\ \tilde{L}^{s_2}_n \\ \tilde{L}^{s_k}_n \end{bmatrix} = \begin{bmatrix} \frac{u_n + c}{\rho c^2}\frac{\partial p}{\partial x_n} + \frac{u_n + c}{c}\frac{\partial u_n}{\partial x_n} \\ \frac{u_n - c}{\rho c^2}\frac{\partial p}{\partial x_n} - \frac{u_n - c}{c}\frac{\partial u_n}{\partial x_n} \\ \frac{u_n}{c}\frac{\partial u_{s_1}}{\partial x_n} \\ \frac{u_n}{c}\frac{\partial u_{s_2}}{\partial x_n} \\ \frac{u_n Y_k}{\rho c^2}\frac{\partial p}{\partial x_n} - \frac{u_n}{\rho}\frac{\partial \rho_k}{\partial x_n} \end{bmatrix}, \tag{18}$$

$$\tilde{L}^*_{s_1} = \begin{bmatrix} \tilde{L}^+_{s_1} \\ \tilde{L}^-_{s_1} \\ \tilde{L}^{s_1}_{s_1} \\ \tilde{L}^{s_2}_{s_1} \\ \tilde{L}^{s_k}_{s_1} \end{bmatrix} = \begin{bmatrix} \frac{u_{s_1}}{\rho c^2}\frac{\partial p}{\partial x_{s_1}} + \frac{u_{s_1}}{c}\frac{\partial u_n}{\partial x_{s_1}} + \frac{\partial u_{s_1}}{\partial x_{s_1}} \\ \frac{u_{s_1}}{\rho c^2}\frac{\partial p}{\partial x_{s_1}} - \frac{u_{s_1}}{c}\frac{\partial u_n}{\partial x_{s_1}} + \frac{\partial u_{s_1}}{\partial x_{s_1}} \\ \frac{1}{\rho c}\frac{\partial p}{\partial x_{s_1}} + \frac{u_{s_1}}{c}\frac{\partial u_{s_1}}{\partial x_{s_1}} \\ \frac{u_{s_1}}{c}\frac{\partial u_{s_2}}{\partial x_{s_1}} \\ \frac{u_{s_1} Y_k}{\rho c^2}\frac{\partial p}{\partial x_{s_1}} - \frac{u_{s_1}}{\rho}\frac{\partial \rho_k}{\partial x_{s_1}} \end{bmatrix}, \tag{19}$$

$$\tilde{L}^*_{s_2} = \begin{bmatrix} \tilde{L}^+_{s_2} \\ \tilde{L}^-_{s_2} \\ \tilde{L}^{s_1}_{s_2} \\ \tilde{L}^{s_2}_{s_2} \\ \tilde{L}^{s_k}_{s_2} \end{bmatrix} = \begin{bmatrix} \frac{u_{s_2}}{\rho c^2}\frac{\partial p}{\partial x_{s_2}} + \frac{u_{s_2}}{c}\frac{\partial u_n}{\partial x_{s_2}} + \frac{\partial u_{s_2}}{\partial x_{s_2}} \\ \frac{u_{s_2}}{\rho c^2}\frac{\partial p}{\partial x_{s_2}} - \frac{u_{s_2}}{c}\frac{\partial u_n}{\partial x_{s_2}} + \frac{\partial u_{s_2}}{\partial x_{s_2}} \\ \frac{u_{s_2}}{c}\frac{\partial u_{s_1}}{\partial x_{s_2}} \\ \frac{1}{\rho c}\frac{\partial p}{\partial x_{s_2}} + \frac{u_{s_2}}{c}\frac{\partial u_{s_2}}{\partial x_{s_2}} \\ \frac{u_{s_2} Y_k}{\rho c^2}\frac{\partial p}{\partial x_{s_2}} - \frac{u_{s_2}}{\rho}\frac{\partial \rho_k}{\partial x_{s_2}} \end{bmatrix}, \tag{20}$$

where (L^+, L^-), (L^{s_1}, L^{s_2}) and L^{s_k} are related to acoustic, vorticity and species-entropy waves, respectively. Combining Eqs. (13) to (17) and using classical thermodynamics relations, additional equations may be derived for completeness:

$$\frac{\partial Y_k}{\partial t} = \tilde{L}^{s_k} - Y_k \tilde{L}^s \quad \text{with} \quad \tilde{L}^s = \sum_{k=1}^{N_s} \tilde{L}^{s_k} \tag{21}$$

$$\frac{\partial \rho}{\partial t} = \rho \tilde{L}^s - \frac{\rho}{2}\left(\tilde{L}^+ + \tilde{L}^-\right) \tag{22}$$

$$\frac{\partial T}{\partial t} = \left[\frac{\rho c^2}{2}\left(\frac{c_v}{c_p} - 1\right)\left(\tilde{L}^+ + \tilde{L}^-\right) - \rho \sum_{k=1}^{N_s} \frac{\partial p}{\partial \rho_k}\Big|_{T,\rho_{j\neq k}} \tilde{L}^{s_k}\right] \Big/ \frac{\partial p}{\partial T}\Big|_{\rho_k} \tag{23}$$

This formulation natively guarantees that $\sum_k \partial Y_k/\partial t = 0$. The different types of inlet and outlet conditions (subsonic, supersonic, *etc.*) are managed with the same procedure than in [27].

Table 2
Mayer's initial conditions.

Investigated cases	Units	Case 3	Case 4
Injection velocity	m/s	4.9	5.4
Injection temperature	K	126.9	137
Injection density	kg/m^3	455.1	163.5
Injection speed of sound	m/s	261	202
Chamber pressure	MPa	3.97	3.98
Chamber temperature	K	298	298

A complete derivation[3] of the boundary conditions treatment is given in Appendix A.

3. Results and discussion

3.1. Single species configuration: Mayer et al.'s experiment

The topic addressed in this study focuses on Mayer et al.'s experiment [1] where a cold nitrogen ($p_c = 3.34$ MPa and $T_c = 126.2$ K) is injected into a warm nitrogen environment under different ambient and injection conditions. The diameter of the injector is $d_{inj} = 2R = 2.2$ mm and the chamber length is 1000 mm with a diameter of 122 mm. For the experimental apparatus, the inlet temperature of the injected fluid can be as low as 90 K and inlet velocities and pressures may vary from 1 to 6 m/s and from 3.95 to 6 MPa, respectively, according to case considered. Cases 3 and 4 in Mayer et al.'s article [1] are under study and correspond to cases on either side of the pseudo-boiling line (Table 2), which is the prolongation of the gas/liquid phase-change line and corresponds to a maximum of constant-pressure heat capacity for a given pressure.

As a consequence, density at the injection plane is almost three times denser for case 3 than for case 4, even if temperatures in both cases are close (10 K of difference). The potential core of fluid injection is then expected to be longer for case 3 than for case 4. The compressibility factor, Z, for inlet conditions is around 0.23 and 0.596 for cases 3 and 4, respectively, but close to unity for ambient fluid.

In Mayer et al.'s configuration, a 2D Raman technique has been used to extract the centerline density profiles for the cases 3 and 4, as well as the evolution of the "half width, half maximum" (HWHM) indicator based on the density along the jet centerline for case 3. These data are quite dispersed with an uncertainty on inlet data (pressure and temperature). For case 3 (see Table 2), Mayer et al. indicates a temperature target of 126.7 K at a pressure of 4 MPa. This leads to an expected density of 465 kg/m^3 that may be recovered with the PR EoS. However, Mayer et al. only reaches a value of 400 kg/m^3 meaning that the temperature might be higher than expected. Indeed, in Fig. 1(a), the experimental point is located at the pseudo-boiling line. A small variation in temperature will lead to large variation in density making experiments and simulations of supercritical flows very tricky. Nevertheless, this density value is captured with the SRK EoS based on the data coming from Mayer et al. as in Table 2. Because of these uncertainties on experimental data both PR and SRK EoS will be used in the LES for comparison.

3D simulations are realized for a domain of calculation defined by $L_x \times L_y \times L_z = 65 \times 30 \times 30$ mm. The mesh arrangement corresponds to $N_x \times N_y \times N_z = 344 \times 184 \times 184 \approx 11.6$ millions of points. Only a small part of the experimental chamber is simulated to save the time of calculation, but the boundary conditions are adapted to still have a representative simulation of the configuration. NSCBC treatment is applied with fixed temperature and velocity at inlet, and prescribed pressure for outlets. Walls are considered as

[3] This work is also the baseline of WENO formulations dealing with real gas effects [42].

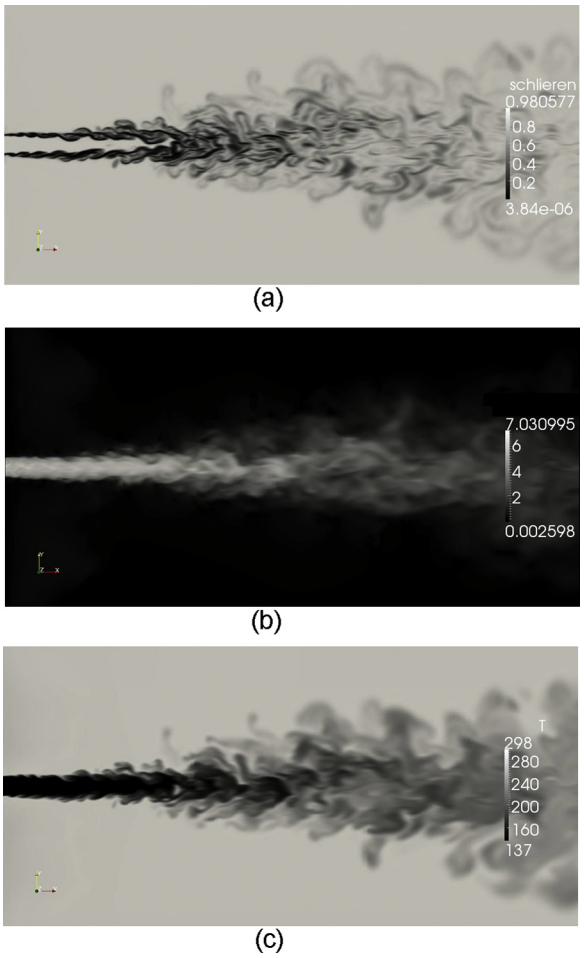

Fig. 2. Mayer et al.'s supercritical jet configuration (case 4): instantaneous flow field.

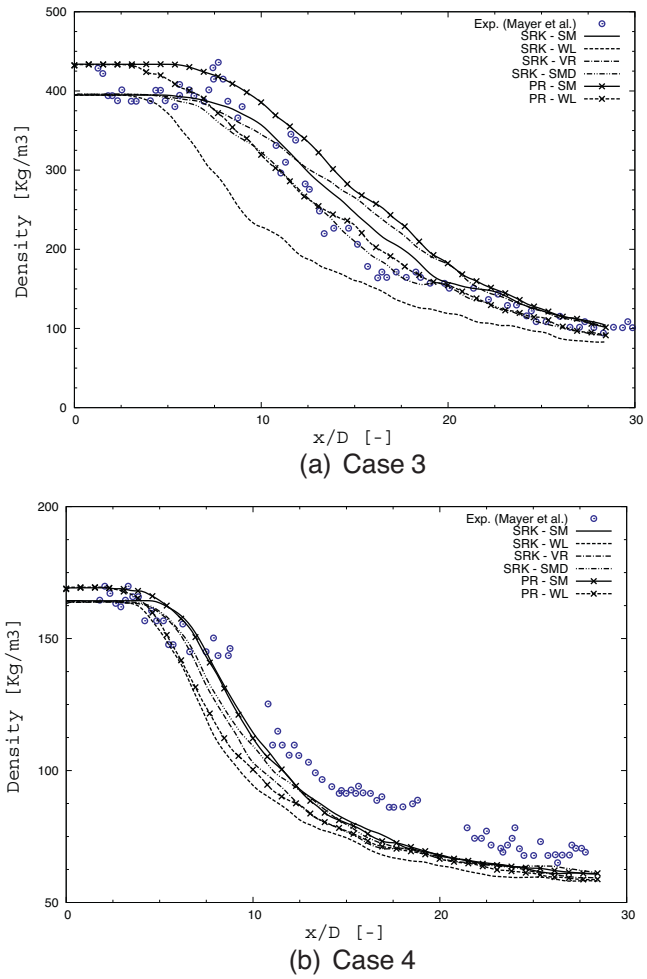

Fig. 3. Mayer et al.'s supercritical jet experiments: centerline density profiles.

adiabatic walls. Injection is given by a turbulent pipe profile (Eqs. (8)) discretized on 34 mesh points.

In Figs. 2, instantaneous flow fields are provided for case 4 (case 3 leading to similar snapshots). In Fig. 2(a) the flow is viewed through a Schlieren image, *i.e.* density gradient. Lower values correspond to high density gradients and are mainly located close to the injection and further downstream in the core jet. The jet enters into the cavity and quickly destabilizes. A part of the light surrounding nitrogen is then very quickly embedded into the main core jet before the jet opening. Some structures observed after one third of the domain, are detaching from the core jet and bear a similarity to those observed in 2D simulations with DNS resolution [28]. They could require here a finer mesh resolution for a very fine tracking of them as they dissolve quite quickly. In Fig. 2(b) and and (c) the jet is viewed through the velocity magnitude and temperature field, respectively. The maximum velocity is found in the injection plane because of the inlet turbulent profile and HIT characteristics. Dense pockets seem to persist in the main core jet and exhibit high speed velocity.

In Figs. 3, simulations are compared to experimental data for density on the jet axis. In both cases, these data are quite dispersed for the first part of the flow. A plateau is observed near the injection plane before a decrease to $\rho(x/D=30)\approx 100\,\mathrm{kg/m^3}$ for case 3 and $\rho(x/D=30)\approx 70\,\mathrm{kg/m^3}$ for case 4, the density of the surrounding fluid being around $45\,\mathrm{kg/m^3}$. The plateau persists longer in the flow for case 3 than for case 4 as it has a higher density value. In Fig. 3(a) simulations of case 3 match very well with experiments whereas in Fig. 3(b), simulations of case 4 under-estimate experiments but still keep the trend. For both cases, a slope break is observed around $x/D\approx 17$ for case 3 and $x/D\approx 15$ for case 4. More precisely, based on the target values given by Mayer et al. for the inlet conditions of case 3, the results with the PR-SM models largely overestimate the experimental data, excepted for $x/D>22$.

Using the PR-WL models leads to have better results ($x/D>12$). However both models fail to describe the near injection process. Switching from PR to SRK EoS, but keeping the two SGS models as previously, grossly switches the results, especially for the first part of the flow where the mixing is less important on the centerline of the jet ($x/D<20$). SRK-SM are the best results obtained and SRK-WL, the worst. Using now the couple SRK-SMD leads to very good results except around $x/D=9$, *i.e.* close to the top of the cold N_2 potential core. For all these combinations of models, only those based on SRK and Smagorinsky SGS models (SM and SMD) are able to reproduce the slope break observed in measurements.

Compared to case 3, the density of case 4 at the injection plane is lighter as the inlet temperature is higher. As a consequence, density calculation coming from both SRK and PR EoS are very close (see Fig. 1(a)). Another global observation is that the simulations follow the same trend and give roughly the same results whatever the sub grid model. For $x/D<7$ all models are equivalent as the experimental data are very dispersed. For $x/D>7$, these models may be grouped into three categories: constant Smagorinsky SGS model used with any EoS gives the best results; at the opposite, the WALE model combined with any EoS leads to the worst results; between both situations, SRK-VR and SRK-SMD are acceptable.

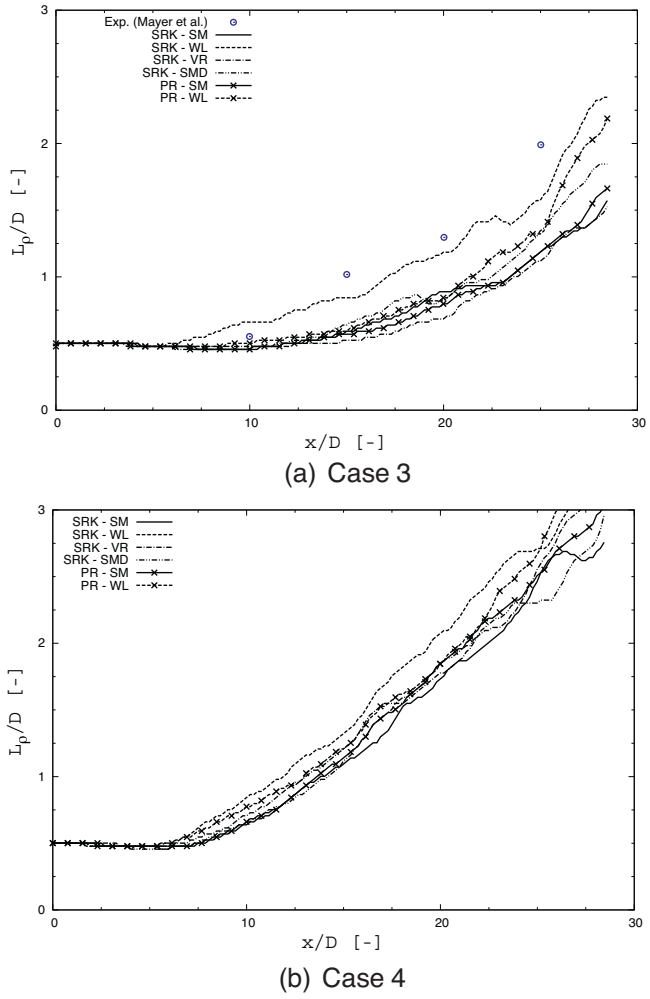

Fig. 4. Mayer et al.'s supercritical jet experiments: spreading rates of jets.

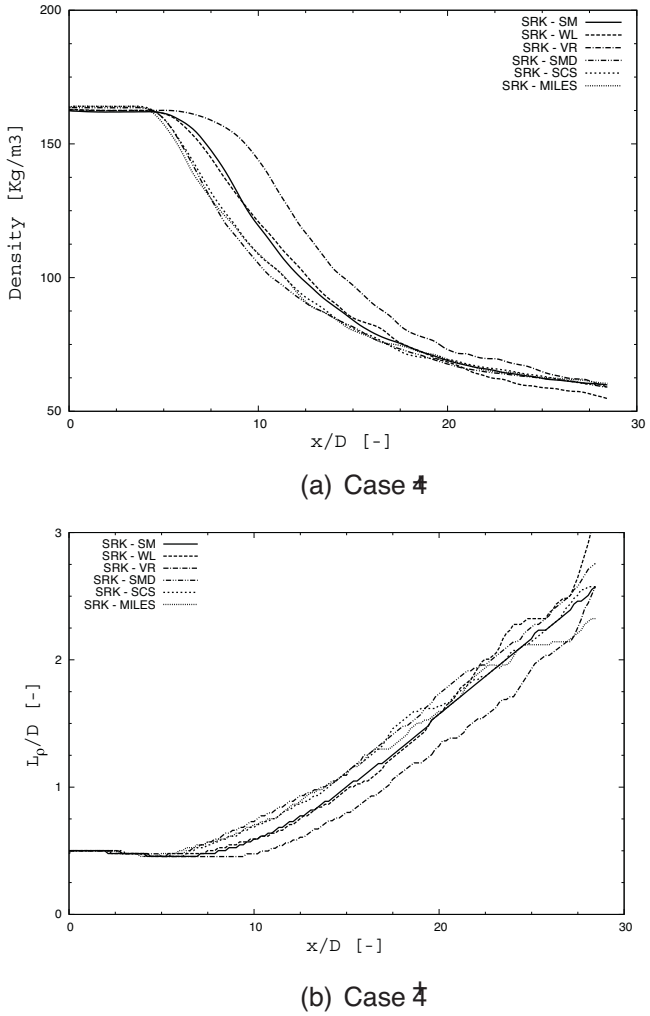

Fig. 5. Mayer et al.'s supercritical jet configuration with higher inlet velocity.

Conclusions can be drawn based on the above observations for both cases 3 and 4: SRK EoS and Smagorinsky models are able to recover both situations. WALE-based models should be avoided even if fairly good results are found for the case 3.

The spreading rates of jets based on density are evaluated using the "half width, half maximum" (HWHM) indicator [4,8,43]. Cross-stream profiles of average density are used to define the HWHM length, L_ρ, of the jet, taken at the median value between dense and light regions along the x-axis (Figs. 4).

Experimental data are only available for case 3. At the injection plane, L_ρ/D is equal to 0.5 as $L_\rho = D/2$. This value persists in the flow as long as the potential core exists. Then the jet opens and L_ρ/D must increase as dense and light fluids mix together. For case 3, the potential core is experimentally observed up to $x/D = 10$ then the jet grossly opens as $L_\rho = 0.1x - 0.5D$, whereas for case 4, the potential core is shorter ($x/D \approx 7.5$) with a jet opening numerically evaluated around $L_\rho = 0.125x - 0.4D$. In Fig. 4(a), the SRK-WL model leads to fairly good results compared to experimental data, but with an underestimated potential core length. All the other combinations of SGS models and EoS yield a longer potential core length but with an acceptable slope for the jet opening. For case 4 (Fig. 4(b)), all the models are gathered and exhibit a similar trend.

In Mayer et al.'s experiments, the inlet velocity is limited to 6 m/s. However, in a real device such as the injectors of a rocket motor engine, the inlet velocity of fuel may reach very high values of the order of 100 m/s. A new case, called case 4$^+$, has then be designed based on the case 4 of Mayer et al.'s configuration, but with a higher inlet velocity: $u = 54$ m/s.

The results for the centerline density profile and L_ρ are displayed in Figs. 5. For case 4, Smagorinsky models were the most capable to reproduce experimental data contrary to the WALE model. For case 4$^+$, both Smagorinsky and WALE models give the same results meaning that great uncertainty still exists on the modeling strategy of turbulence for small mass flow rate, the choice becoming less crucial for higher mass flow rate. The VR model shows a longer potential dense core contrary to the SMD and scale-similarity (SCS) [44] models or with the Monotone Integrated LES (MILES) approach [45]. Actually, the low bulk velocities (around 5 m/s) of Mayer experiment is clearly far away from velocity encountered in real systems (between 5 and 100 m/s). Our conclusion is that additional experimental data are required to really conclude about turbulence modeling.

In Eq. (5), $\nabla\bar{p}$ can be modeled using the first order of the Taylor expansion (FOC *i.e. First Order Correction* model) [11]:

$$\frac{\partial \overline{p}}{\partial x_i} = \frac{\partial}{\partial x_i}\left[\overline{p(\bar{\phi})} + \left.\frac{\partial p}{\partial \phi_l}\right|_{\phi=\bar{\phi}} (\bar{\phi}_l - \bar{\bar{\phi}}_l)\right], \tag{24}$$

with $\phi = \{\rho u_i, \rho E, \rho Y_k\} = \{\phi_l\}$. In Eq. (24), any quantity $\bar{Q}$ is the LES solution and $\bar{\bar{Q}}$ is the filtered LES solution. Applying this model to our simulations makes them unstable and $\bar{p}$ is then classically modeled as $\overline{p(Q)} = p(\bar{Q})$.

3.2. Mascotte test bench

To study the mixing under supercritical conditions, a co-axial injector is numerically simulated with the conditions encountered in the Mascotte test bench [46–48]. Two variants of the liquid oxygen/methane co-axial injector are available. In both configurations, the liquid oxygen ($T_{O_2} \approx 90$ K) is fed through the central cylindrical channel whereas the gaseous or liquid methane is supplied through the outer annular channel. No turbulence intensity of the methane jet at the inlet is specified as the methane stream velocity is substantial, *i.e.* of the order of 100 m/s. Only the case with gaseous methane is studied hereafter, *i.e.* the inlet temperature is near 290 K. The high-pressure Mascotte test-bench combustion chamber has a square section of $L_y \times L_z = 55^2$ mm^2 which is around five times the injector diameter. Between the LO_x and methane streams, a ratio of 30 and 50 is found for the density and the velocity, respectively, leading to a configuration which is a real challenge for numerical codes.

In the present study, the dimension used in the simulation are $L_x = 75$, $L_y = 25$ and $L_z = 25$ mm discretized with $N_x = 432$, $N_y = 384$ and $N_z = 384$ cells, respectively. The flow inside the inlet tubes is not simulated. Adiabatic walls are considered. The CFL number is set to 0.95, the Fourier number is 0.2 and the Prandtl number is unity. SRK EoS is used with either the SM or SMD models for subgrid turbulence viscosity.

In Fig. 6, an instantaneous snapshot is provided based either on the Q-criterion that describes coherent flow structures and the mixing variable defined as $Y_{CH_4} \times Y_{O_2} \times 4$. In Fig. 6(a), the Q-criterion, $Q = 0.5(|\Omega|^2 - |S|^2)$ with $S = 0.5(\nabla u + (\nabla u)^T)$ and

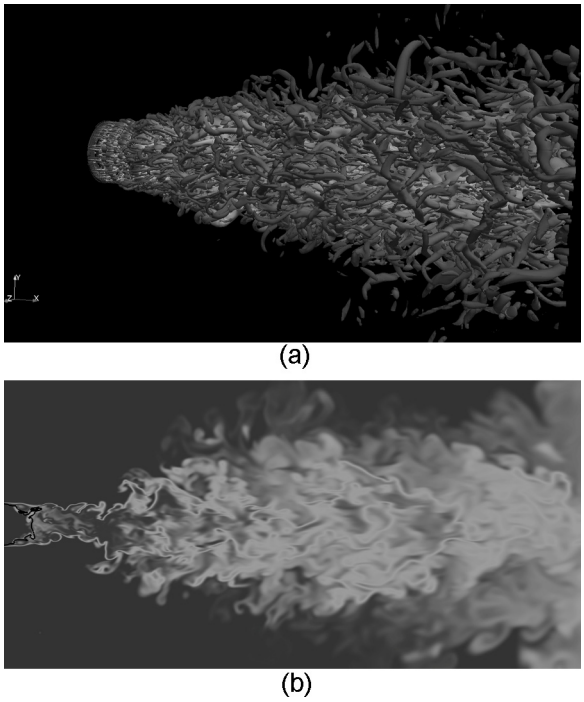

Fig. 6. Visualization of the instantaneous flow field: (a) Q-criterion and (b) mixing variable.

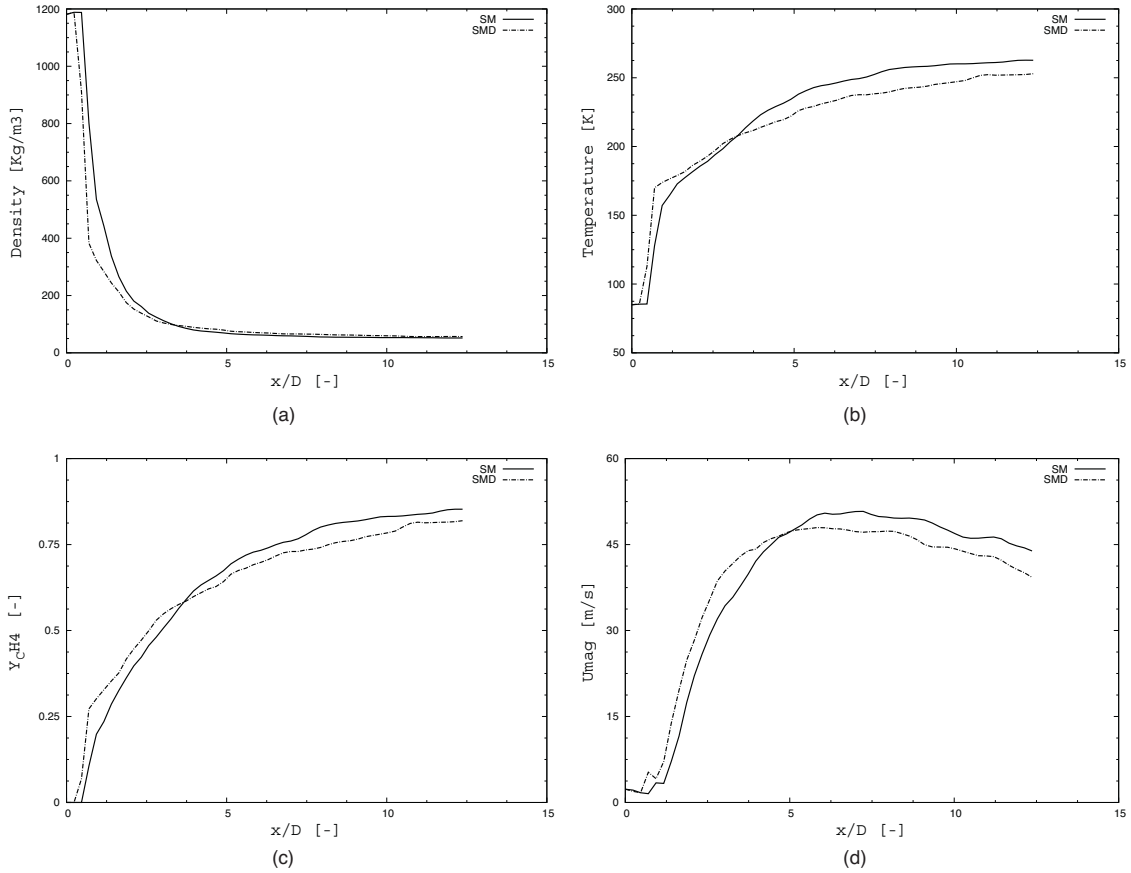

Fig. 7. Centerline density profile (a), temperature (b), methane mass fraction (c) and velocity magnitude (d).

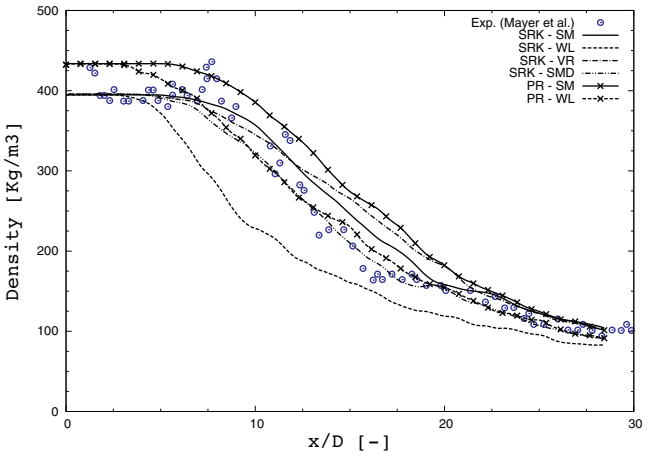

Fig. 8. Evolution of the HWHM based on density and methane mass fraction along the jet centerline.

$\Omega = 0.5(\nabla u - (\nabla u)^T)$, set to the critical value of $Q_c = 10^8 = (U_{CH_4}/D_{O_2})$ indicates a very turbulent flow. Indeed, the Reynolds number based on the methane stream is above 1.10^6. In Fig. 6(b), a strong mixing is also observed. Dark gray color corresponds either to pure LO_x or CH_4 streams; light gray corresponds to perfect mixing. The dense LO_x core is rapidly destroyed because the shear layer is under the constraint of strong density and velocity gradients. As a consequence the stoichiometric iso-line (black line in Fig. 6(b)) is very close to the injector.

Mean centerline profiles of density, temperature, methane mass fraction and velocity are given in Fig. 7. SM and SMD SGS models have been used. The dense LO_x core is clearly identifying as a short plateau is observed close to the injector face. Then a slope change appears corresponding to strong mixing followed by a slight evolution of the different variables. Density, temperature and species mass fractions reach limit value whereas the velocity reaches a maximum around $x/D \approx 6$ before decreasing. Using the SMD SGS model leads to a slightly stiffer slope as the level of turbulent viscosity is less important than with the classical SM SGS model.

Centerline evolution of the HWHM are shown in Fig. 8 for density (L_ρ) and methane mass fraction ($L_{Y_{CH_4}}$) used with SM and SMD SGS models. These variables are thermodynamically linked and have a similar evolution on the domain of simulation. Nevertheless, in the dense LO_x core, density profiles first decrease before increasing. This behavior is due to the species and energy diffusion and the strong non-linear evolution of density as a function of temperature through the SRK EoS.

4. Conclusion

A code called SiTCom-B has been developed to run real-gas configurations such as injection of supercritical fluid. SiTCom-B thermodynamics has been validated against NIST data and simulation of Mayer et al.'s experiments have been successfully realized with standard model for sub-grid viscosity and light mesh. Soave–Redlich–Kwong EoS and Dynamic Smagorinsky SGS models seem to be the most convenient couple to reproduce such experiment. Surprising effect appears when increasing the bulk velocity as conclusion on models impacts can be inverted even if for higher injection velocities the subgrid model has less importance. Actually, more advanced comparison on fluctuations of density or temperature is unfeasible due to the lack of experimental data, DNS of realistic configuration being still out of scope due to CPU time. The study of species mixing under supercritical conditions has been realized through the simulation of the MASCOTTE test-bench. The dense LO_x core is totally shred after one diameter of length because of the deep density and velocity gradients.

Based on our results on the MASCOTTE test-bench, future works will be focused on combustion in the case of co-axial injection of methane and LO_x.

Acknowledgments

Computations were performed using HPC resources from CRIHAN and GENCI [CCRT/CINES/IDRIS].

Appendix A. Three-dimensional NSCBC treatment for general fluid flows

A.1. Useful thermodynamic relations

Developing a general treatment of the three-dimensional Navier–Stokes boundary conditions for multicomponent reactive fluid flows featuring any equation of state requires a particular attention to partial derivatives.

Considering the pressure as a function of $N_s + 1$ variables, its differential form $p = p(T, \rho_k)$ is written:

$$dp = \left.\frac{\partial p}{\partial T}\right|_{\rho_k} dT + \sum_{k=1}^{N_s} \left.\frac{\partial p}{\partial \rho_k}\right|_{T,\rho_{k\neq j}} d\rho_k, \tag{A.1}$$

where T is the temperature and $\rho_k = \rho Y_k$ with ρ, density, and Y_k, the kth species mass fraction in the N_s species pool. Assuming that $\sum_k Y_k = 1$, the differential form of ρ_k, $d\rho_k = Y_k d\rho + \rho dY_k$, is introduced into Eq. (A.1) to lead to

$$dp = \left.\frac{\partial p}{\partial T}\right|_{\rho_k} dT + \sum_{k=1}^{N_s} Y_k \left.\frac{\partial p}{\partial \rho_k}\right|_{T,\rho_{k\neq j}} d\rho + \rho \sum_{k=1}^{N_s} \left.\frac{\partial p}{\partial \rho_k}\right|_{T,\rho_{k\neq j}} dY_k. \tag{A.2}$$

The differential form of the pressure considered as a function of $N_s + 2$ variables $P(\rho, T, Y_k)$ is written

$$dp = \left.\frac{\partial P}{\partial T}\right|_{\rho,Y_k} dT + \left.\frac{\partial P}{\partial \rho}\right|_{T,Y_k} d\rho + \sum_{k=1}^{N_s} \left.\frac{\partial P}{\partial Y_k}\right|_{T,\rho,Y_{k\neq j}} dY_k. \tag{A.3}$$

If $\sum_k Y_k = 1$ then $p(T, \rho_k) = P(\rho, T, Y_k)$, and by identification:

$$\left.\frac{\partial p}{\partial T}\right|_{\rho_k} = \left.\frac{\partial P}{\partial T}\right|_{\rho,Y_k}, \quad \sum_{k=1}^{N_s} Y_k \left.\frac{\partial p}{\partial \rho_k}\right|_{T,\rho_{k\neq j}} = \left.\frac{\partial P}{\partial \rho}\right|_{T,Y_k} \tag{A.4}$$

$$\text{and} \quad \rho \sum_{k=1}^{N_s} \left.\frac{\partial p}{\partial \rho_k}\right|_{T,\rho_{k\neq j}} = \sum_{k=1}^{N_s} \left.\frac{\partial P}{\partial Y_k}\right|_{T,\rho,Y_{k\neq j}}. \tag{A.5}$$

Similarly, Meng and Yang [30] showed for enthalpy, h, that

$$\left.\frac{\partial h}{\partial p}\right|_{\rho_k} = \frac{1}{\rho} + C_v \left[\left.\frac{\partial p}{\partial T}\right|_{\rho_k}\right]^{-1}, \tag{A.6}$$

and

$$\left.\frac{\partial h}{\partial \rho_k}\right|_{p,\rho_{k\neq j}} = C_{T,k} - \frac{p}{\rho^2} - C_v \left[\left.\frac{\partial p}{\partial T}\right|_{\rho_k}\right]^{-1} \left.\frac{\partial p}{\partial \rho_k}\right|_{T,\rho_{k\neq j}}, \tag{A.7}$$

with C_v and $C_{T,k}$ linked to the internal energy, e, as

$$C_v = \left.\frac{\partial e}{\partial T}\right|_{\rho_k} \quad \text{and} \quad C_{T,k} = \sum_{k=1}^{N_s} \left.\frac{\partial e}{\partial \rho_k}\right|_{T,\rho_{k\neq j}}. \tag{A.8}$$

In addition, Meng and Yang define the heat capacity at constant pressure as

$$C_p = C_v - \frac{1}{\rho}\left.\frac{\partial p}{\partial T}\right|_{\rho_k} \left.\frac{\partial \rho}{\partial p}\right|_{T,Y_k} \left[\left(\sum_{k=1}^{N_s} Y_k(\rho C_{T,k} + e)\right) - e - \frac{p}{\rho}\right], \tag{A.9}$$

that can be recast in

$$C_p = \frac{1}{\rho}\sum_{k=1}^{N_s}\left[C_v + \left(\frac{p}{\rho^2} - C_{T,k}\right)\left.\frac{\partial p}{\partial T}\right|_{\rho_k} \left.\frac{\partial \rho}{\partial p}\right|_{T,Y_k}\right]\rho_k. \tag{A.10}$$

A.2. NSCBC-3D treatment

Treating the characteristic boundary conditions must be done in the local basis $\mathcal{B} = (x_n, x_{s_1}, x_{s_2})$ that is obtained by applying a rotation onto the classical cartesian basis $\mathcal{E} = (x_1, x_2, x_3)$. x_n is the unit vector normal to the boundary surface, pointing in the outward direction and the two other vectors x_{s_1} and x_{s_2} are chosen so that $\mathcal{B}$ is a direct orthonormal basis. In such basis, the Navier–Stokes equations for multicomponent reactive flows are written:

$$\frac{\partial U}{\partial t} + \frac{\partial F^j}{\partial x_j} = 0 \tag{A.11}$$

where $U = [\rho u_n, \rho u_{s_1}, \rho u_{s_2}, \rho e_t, \rho Y_k]^T$ is the vector of conservative variables. u_i are the velocities in $\mathcal{B}$, ρe_t is the total energy decomposed as the sum of the internal ($\rho e = \rho h - p$) and kinetic ($e_c = \rho u^2/2$) energies. h is the enthalpy of the mixture. F^j represents the conservative variables flux vectors and is given by:

$$F^n = \begin{bmatrix} \rho u_n u_n + p \\ \rho u_n u_{s_1} \\ \rho u_n u_{s_2} \\ \rho u_n e_t + u_n p \\ \rho u_n Y_k \end{bmatrix} \tag{A.12}$$

$$F^{s_1} = \begin{bmatrix} \rho u_{s_1} u_n \\ \rho u_{s_1} u_{s_1} + p \\ \rho u_{s_1} u_{s_2} \\ \rho u_{s_1} e_t + u_{s_1} p \\ \rho u_{s_1} Y_k \end{bmatrix}, \quad F^{s_2} = \begin{bmatrix} \rho u_{s_2} u_n \\ \rho u_{s_2} u_{s_1} \\ \rho u_{s_2} u_{s_2} + p \\ \rho u_{s_2} e_t + u_{s_2} p \\ \rho u_{s_2} Y_k \end{bmatrix} \tag{A.13}$$

Introducing the vector of primitive variables $V = [u_n, u_{s_1}, u_{s_2}, p, \rho_k]^T$ into Eq. (A.11) leads to:

$$\frac{\partial V}{\partial t} + A_j \frac{\partial V}{\partial x_j} = 0, \tag{A.14}$$

where $A_j = M^{-1}C_j$, with the two jacobian matrices $M = \partial U/\partial V$ and $C_j = \partial F^j/\partial V$. The matrix A_n is written:

$$A_n = \begin{pmatrix} u_n & 0 & 0 & 1/\rho & 0 & \cdots & 0 \\ 0 & u_n & 0 & 0 & 0 & \cdots & 0 \\ 0 & 0 & u_n & 0 & 0 & \cdots & 0 \\ \rho\tilde{c}^2 & 0 & 0 & u_n & 0 & \cdots & 0 \\ \rho_1 & 0 & 0 & 0 & u_n & \cdots & 0 \\ \vdots & 0 & 0 & 0 & 0 & \ddots & 0 \\ \rho_{N_s} & 0 & 0 & 0 & 0 & \cdots & u_n \end{pmatrix} \tag{A.15}$$

with the modified speed of sound

$$\rho\tilde{c}^2 = \frac{p + \rho e_t - \sum_k \rho_k \mathcal{M}_{\rho_k}}{\mathcal{M}_p}. \tag{A.16}$$

$\mathcal{M}_{\rho_k}$ and $\mathcal{M}_p$ are defined as:

$$\mathcal{M}_{\rho_k} = \left.\frac{\partial(\rho e_t)}{\partial \rho_k}\right|_{p,u_1,u_2,u_3,\rho_{j\neq k}} = h + \rho \left.\frac{\partial h}{\partial \rho_k}\right|_{p,\rho_{j\neq k}} + e_c \tag{A.17}$$

$$\mathcal{M}_p = \left.\frac{\partial(\rho e_t)}{\partial p}\right|_{u_1,u_2,u_3,\rho_k} = \rho \left.\frac{\partial h}{\partial p}\right|_{\rho_k} - 1 \tag{A.18}$$

Eq. (A.16) then becomes:

$$\tilde{c}^2 = \frac{-\sum_k \rho_k \left.\frac{\partial h}{\partial \rho_k}\right|_{p,\rho_{j\neq k}}}{\rho \left.\frac{\partial h}{\partial p}\right|_{\rho_k} - 1}. \tag{A.19}$$

In Eq. (A.19), the numerator can be expressed using Eqs. (A.4) and (A.7):

$$-\sum_{k=1}^{N_s} \rho_k \left.\frac{\partial h}{\partial \rho_k}\right|_{p,\rho_{j\neq k}} = \left[\sum_{k=1}^{N_s}\left(-C_{T,k} + \frac{p}{\rho^2}\right)\rho_k\right] + \rho C_v \left.\frac{\partial p}{\partial \rho}\right|_{T,Y_k}. \tag{A.20}$$

Introducing Eq. (A.10) into Eq. (A.20) leads to:

$$-\sum_{k=1}^{N_s} \rho_k \left.\frac{\partial h}{\partial \rho_k}\right|_{p,\rho_{j\neq k}} = \rho C_p \left.\frac{\partial p}{\partial \rho}\right|_{T,Y_k} \left[\left.\frac{\partial p}{\partial T}\right|_{\rho_k}\right]^{-1}. \tag{A.21}$$

Using Eq. (A.6) to express the denominator of Eq. (A.19) leads to

$$\tilde{c}^2 = \frac{C_p}{C_v}\left.\frac{\partial p}{\partial \rho}\right|_{T,Y_k}, \tag{A.22}$$

which is the definition of the speed of sound, meaning that the above derivation is consistent.

Matrixes A_{s_1} and A_{s_2} are written:

$$A_{s_1} = \begin{pmatrix} u_{s_1} & 0 & 0 & 0 & 0 & \cdots & 0 \\ 0 & u_{s_1} & 0 & 1/\rho & 0 & \cdots & 0 \\ 0 & 0 & u_{s_1} & 0 & 0 & \cdots & 0 \\ 0 & \rho\tilde{c}^2 & 0 & u_{s_1} & 0 & \cdots & 0 \\ 0 & \rho_1 & 0 & 0 & u_{s_1} & \cdots & 0 \\ 0 & \vdots & 0 & 0 & 0 & \ddots & 0 \\ 0 & \rho_{N_s} & 0 & 0 & 0 & \cdots & u_{s_1} \end{pmatrix} \tag{A.23}$$

$$A_{s_2} = \begin{pmatrix} u_{s_2} & 0 & 0 & 0 & 0 & \cdots & 0 \\ 0 & u_{s_2} & 0 & 0 & 0 & \cdots & 0 \\ 0 & 0 & u_{s_2} & 1/\rho & 0 & \cdots & 0 \\ 0 & 0 & \rho\tilde{c}^2 & u_{s_2} & 0 & \cdots & 0 \\ 0 & 0 & \rho_1 & 0 & u_{s_2} & \cdots & 0 \\ 0 & 0 & \vdots & 0 & 0 & \ddots & 0 \\ 0 & 0 & \rho_{N_s} & 0 & 0 & \cdots & u_{s_2} \end{pmatrix} \tag{A.24}$$

Introducing the differential form of the normalized primitive variables $d\widetilde{V} = [du_n/c, du_{s_1}/c, du_{s_2}/c, dp/(\rho c^2), d\rho_k/\rho]^T$ into Eq. (A.14) leads to:

$$\frac{\partial \widetilde{V}}{\partial t} + \tilde{A}_j \frac{\partial \widetilde{V}}{\partial x_j} = 0, \tag{A.25}$$

with $dV = Pd\widetilde{V}$ and $\tilde{A}_j = P^{-1}A_jP$. Defining the differential form of the normalized characteristic variables as

$$\begin{aligned} d\widetilde{W}^{+} &= \frac{dp}{\rho c^2} + \frac{du_n}{c}, \\ d\widetilde{W}^{-} &= \frac{dp}{\rho c^2} - \frac{du_n}{c}, \\ d\widetilde{W}^{s_1} &= \frac{du_{s_1}}{c}, \\ d\widetilde{W}^{s_2} &= \frac{du_{s_2}}{c}, \\ d\widetilde{W}^{s_k} &= \frac{Y_k dp}{\rho c^2} - \frac{d\rho_k}{\rho}, \end{aligned} \tag{A.26}$$

Euler equations (Eq. (A.25)) can be written

$$\frac{\partial \widetilde{W}}{\partial t} + \sum \tilde{L}_j = 0, \tag{A.27}$$

with $d\widetilde{W} = K.d\widetilde{V}$ and $\tilde{L}_j = K\tilde{A}_jK^{-1}\partial\widetilde{W}/\partial x_j$, or

$$\frac{\partial \widetilde{V}}{\partial t} + \sum K^{-1}\tilde{L}_j = 0. \tag{A.28}$$

$\tilde{L}_j = (\tilde{L}_j^+, \tilde{L}_j^-, \tilde{L}_j^{s_1}, \tilde{L}_j^{s_2}, \tilde{L}_j^{s_k})^T$ are given in Eqs. (18–20) and lead to the system of Eqs. (13–17). Dealing with the boundary conditions consists of managing the ingoing and outgoing waves ($\tilde{L}_n$) of the domain of calculation. $\tilde{L}_{s_1}$ and $\tilde{L}_{s_2}$ are not affected by boundary conditions as they travel transversally to the boundary face.

To treat the different types of boundary conditions, a procedure with a 'reference' value is used for the implementation into SiT-ComB numerical code. Each primitive variable ϕ, with $\phi = (u_i, p, Y_k, T)^T$, from Eqs. (13–17) and Eqs. (21–23) may be written, if required,

$$\frac{\partial \phi}{\partial t} = -\frac{\Delta\phi}{\tau_\phi}, \quad \text{with} \quad \Delta\phi = \phi^{cell} - \phi^{ref}. \tag{A.29}$$

ϕ^{cell} and ϕ^{ref} are the computed and reference or target values, respectively. τ_ϕ are the relaxation parameters.

The following waves expressions must be set at the inlet/outlet according to chosen boundary conditions type:

- **Supersonic outlet:** all the waves are outgoing meaning that the wave strength are determined from the interior points of the domain of calculation.
- **Supersonic inlet:** all the waves are coming from outside the domain and must be imposed by the boundary conditions.

$$\begin{aligned} \tilde{L}_n^+ &= \tau_p^{-1}\frac{\Delta p}{\rho c^2} + \tau_{u_n^{-1}}\frac{\Delta u_n}{c} \\ \tilde{L}_n^- &= \tau_p^{-1}\frac{\Delta p}{\rho c^2} - \tau_{u_n^{-1}}\frac{\Delta u_n}{c} \\ \tilde{L}_n^{s_1} &= \tau_v^{-1}\frac{\Delta u_{s_1}}{c} \\ \tilde{L}_n^{s_2} &= \tau_w^{-1}\frac{\Delta u_{s_2}}{c} \\ \tilde{L}_n^{s_k} &= Y_k\tilde{L}_n^s - \tau_Y^{-1}\Delta Y_k \\ \tilde{L}_n^s &= \left(1 - \frac{C_p}{C_v}\right)\tau_p^{-1}\frac{\Delta p}{\rho c^2} + \left.\frac{\partial p}{\partial T}\right|_{\rho_k}\frac{C_p}{C_v}\tau_T^{-1}\frac{\Delta T}{\rho c^2} \\ &\quad + \frac{C_p}{C_v}\frac{1}{c^2}\tau_Y^{-1}\sum_{k=1}^{N_s}\left.\frac{\partial p}{\partial \rho_k}\right|_{T,\rho_{k\neq j}}\Delta Y_k \end{aligned}$$

- **Subsonic outlet:** all the waves are outgoing, except $\tilde{L}_n^-$, meaning that the wave strength are determined from the interior points of the domain of calculation.
  - Non-reflecting (NR) outlet:

$$\tilde{L}_n^- = \tilde{L}_n^{-,NR} + 2\tau_p^{-1}\frac{\Delta p}{\rho c^2} \tag{A.30}$$

is used for a pressure-based formulation, and

$$\tilde{L}_n^- = \tilde{L}_n^{-,NR} - 2\tau_{u_n^{-1}}\frac{\Delta u_n}{c} \tag{A.31}$$

is used for a velocity-based formulation, with

$$\tilde{L}_n^{-,NR} = (\beta - 1)(\tilde{L}_{s_1}^- + \tilde{L}_{s_2}^-), \tag{A.32}$$

The coefficient $\beta \in [0, 1]$. $\beta = 1$ corresponds to the Poinsot–Lele NSCBC-1D formulation [49], $\beta = 0$ is the NSCBC-3D formulation of Thompson [50,51], and $\beta \in]0, 1[$ is the NSCBC-3D formulation of Lodato et al. [27] where β can be specified by the user or linked to the local Mach number or its maximum.

  - Reflecting (R) outlet:

$$\tilde{L}_n^- = \tilde{L}_n^{-,R} + 2\tau_p^{-1}\frac{\Delta p}{\rho c^2} \tag{A.33}$$

is used for a pressure-based formulation, and

$$\tilde{L}_n^- = \tilde{L}_n^{-,R} - 2\tau_{u_n^{-1}}\frac{\Delta u_n}{c} \tag{A.34}$$

is used for a velocity-based formulation, with

$$\tilde{L}_n^{-,R} = -(\tilde{L}_n^+ + \tilde{L}_{s_1}^+ + \tilde{L}_{s_2}^+) - (\tilde{L}_{s_1}^- + \tilde{L}_{s_2}^-). \tag{A.35}$$

- **Subsonic inlet:** In this case, the waves $\tilde{L}_n^s$, $\tilde{L}_n^{s_1}$, $\tilde{L}_n^{s_2}$ and $\tilde{L}_n^-$ are coming in the domain from the exterior: they must be prescribed by the boundary conditions. On the other hand, the wave $\tilde{L}_n^+$ is leaving the domain and thus must be left unchanged.
  - Non-reflecting (NR) intlet:

$$\tilde{L}_n^- = \tilde{L}_n^{-,NR} - 2\tau_{u_n}^{-1}\frac{\Delta u_n}{c}$$

$$\tilde{L}_n^{s_1} = \tilde{L}_n^{s_1,NR} + \tau_{u_{s_1}}^{-1}\frac{\Delta u_{s_1}}{c}$$

$$\tilde{L}_n^{s_2} = \tilde{L}_n^{s_2,NR} + \tau_{u_{s_2}}^{-1}\frac{\Delta u_{s_2}}{c}$$

$$\tilde{L}_n^{s_k} = \tilde{L}_n^{s_k,NR} - \tau_Y^{-1}\Delta Y_k + Y_k\left(\frac{c_p}{c_v}-1\right)\tau_{u_n}^{-1}\frac{\Delta u_n}{c} + Y_k\left.\frac{\partial p}{\partial T}\right|_{\rho_k}\frac{c_p}{c_v}\tau_T^{-1}\frac{\Delta T}{\rho c^2} + Y_k\frac{c_p}{c_v}\frac{\Delta Y_k}{c^2}\tau_Y^{-1}\sum_{k=1}^{N_s}\left.\frac{\partial p}{\partial \rho_k}\right|_{T,\rho_{k\neq j}}$$

  with $\tilde{L}_n^{*,NR} = (\beta-1)(\tilde{L}_{s_1}^* + \tilde{L}_{s_2}^*)$.
  - Reflecting (R) intlet:

$$\tilde{L}_n^- = (\tilde{L}_n^+ + \tilde{L}_{s_1}^+ + \tilde{L}_{s_2}^+) - (\tilde{L}_{s_1}^- + \tilde{L}_{s_2}^-) - 2\tau_{u_n}^{-1}\frac{\Delta u_n}{c}$$

$$\tilde{L}_n^{s_1} = -(\tilde{L}_{s_1}^{s_1} + \tilde{L}_{s_1}^{s_2}) + \tau_{u_{s_1}}^{-1}\frac{\Delta u_{s_1}}{c}$$

$$\tilde{L}_n^{s_2} = -(\tilde{L}_{s_2}^{s_1} + \tilde{L}_{s_2}^{s_2}) + \tau_{u_{s_2}}^{-1}\frac{\Delta u_{s_2}}{c}$$

$$\tilde{L}_n^{s_k} = -(\tilde{L}_{s_k}^{s_1} + \tilde{L}_{s_k}^{s_2}) - \tau_Y^{-1}\Delta Y_k + Y_k\left(\frac{c_p}{c_v}-1\right)\tau_{u_n}^{-1}\frac{\Delta u_n}{c} + Y_k\left.\frac{\partial p}{\partial T}\right|_{\rho_k}\frac{c_p}{c_v}\tau_T^{-1}\frac{\Delta T}{\rho c^2} + Y_k\frac{c_p}{c_v}\frac{\Delta Y_k}{c^2}\tau_Y^{-1}\sum_{k=1}^{N_s}\left.\frac{\partial p}{\partial \rho_k}\right|_{T,\rho_{k\neq j}}$$

References

[1] W. Mayer, J. Telaar, R. Branam, G. Schneider, J. Hussong, Raman measurements of cryogenic injection at supercritical pressure, Heat and Mass Transfer 39 (2003) 709–719.
[2] S. Candel, M. Juniper, S. Singla, S. Scouflaire, C. Rolon, Structure and dynamics of cryogenic flames at supercritical pressure, Combustion Science and Technology 178 (2006) 161–192.
[3] J. Oefelein, L. Lacaze, Low-temperature injection dynamics and turbulent flame structure in high-pressure supercritical flows, in: 23rd ICDERS Conf, 2011.
[4] M. Oschwald, A. Schik, Supercritical nitrogen free jet investigated by spontaneous raman scattering, Experiments in Fluids 27 (1999) 497–506.
[5] M. Oschwald, M. Micci, Spreading angle and centerline variation of density of supercritical nitrogen jets, Atomization and Sprays 12 (2002) 91–106.
[6] B. Chehroudi, D. Talley, E. Coy, Visual characteristics and initial growth rates of round cryogenic jets at subcritical and supercritical pressures, Physics of Fluids 14 (2002) 850–861.
[7] B. Chehroudi, R. Cohn, D. Talley, Cryogenic shear layers: experiments and phenomenological modeling of the initial growth rate under subcritical and supercritical conditions, International Journal of Heat and Fluid Flow 23 (2002) 554–563.
[8] R. Branam, W. Mayer, Characterization of cryogenic injection at supercritical pressure, Journal of Propulsion and Power 19 (2003) 342–355.
[9] C. Segal, S. Polikhov, Subcritical to supercritical mixture, Physics of Fluids 20 (2008) 052101.
[10] A. Conley, A. Vaidyanathan, C. Segal, Heat flux measurements for a GO_2/GH_2 single element, shear injector, Journal of Spacecraft and Rockets 44 (2007) 633–639.
[11] E. Taskinoglu, J. Bellan, A posteriori study using a dns database describing fluid disintegration and binary-species mixing under supercritical pressure: heptane and nitrogen, Journal of Fluid Mechanics 645 (2010) 211–254.
[12] J. Oefelein, V. Yang, Modeling high-pressure mixing and combustion processes in liquid rocket engines, Journal of Propulsion and Power 14 (1998) 843–857.
[13] N. Zong, V. Yang, Cryogenic fluid jets and mixing layers in transcritical and supercritical environments, Physics of Fluids 16 (12) (2004) 4248–4261.
[14] N. Zong, H. Meng, S.-Y. Hsieh, V. Yang, A numerical study of cryogenic fluid injection and mixing under supercritical conditions, Combustion Science and Technology 178 (2006) 193–227.
[15] T. Schmitt, L. Selle, A. Ruiz, B. Cuenot, Large-eddy simulation of supercritical pressure round jets, American Institute of Aeronautics and Astronautics Journal 48 (2010) 2133–2144.
[16] J. Smagorinsky, General circulation experiments with the primitive equations, Monthly Weather Review 91 (1963) 99–164.
[17] F. Nicoud, F. Ducros, Subgrid-scale stress modelling based on the square of the velocity gradient tensor., Flow, Turbulence and Combustion 62 (3) (1999) 183–200.
[18] R. Miller, J. Bellan, Direct numerical simulation of a confined three-dimensional gas mixing layer with one evaporating hydrocarbon-droplet laden stream, Journal of Fluid Mechanics 384 (1998) 293–338.
[19] R. Miller, K. Harstad, J. Bellan, Direct numerical simulations of supercritical fluid mixing layers applied to heptane–nitrogen, Journal of Fluid Mechanics 436 (2001) 1–39.
[20] N. Okong'o, J. Bellan, Consistent large-eddy simulation of a temporal mixing layer laden with evaporating drops. Part 1. Direct numerical simulation, formulation and a priori analysis, Journal of Fluid Mechanics 499 (2004) 1–47.
[21] N. Okong'o, K. Harstad, J. Bellan, Direct numerical simulations of O_2/H_2 temporal mixing layers under supercritical conditions, American Institute of Aeronautics and Astronautics Journal 40 (2002) 914–926.
[22] J. Oefelein, Thermophysical characteristics of shear-coaxial LO_x-h2 flames at supercritical pressure, Proceedings of the Combustion Institute 30 (2005) 2929–2937.
[23] B. Poling, J. Prausnitz, J. O'Connell, The Properties of Gases and Liquids, 5th ed., McGraw Hill, 2001.
[24] P. Domingo, L. Vervisch, K. Bray, Partially premixed flamelets in les of non-premixed turbulent combustion, Combustion Theory and Model. 6 (4) (2002) 529–551.
[25] P. Domingo, L. Vervisch, S. Payet, R. Hauguel, Dns of a premixed turbulent V flame and LES of a ducted flame using a FSD-PDF subgrid scale closure with FPI-tabulated chemistry, Combustion and Flame 143 (2005) 566–586.
[26] P. Domingo, L. Vervisch, D. Veynante, Large-eddy simulation of a lifted methane jet flame in a vitiated coflow, Combustion and Flame 152 (2008) 415–432.
[27] G. Lodato, L. Vervisch, P. Domingo, Three-dimensional boundary conditions for direct and large-eddy simulation of compressible viscous flows, Journal of Computational Physics 227 (2008) 5105–5143.
[28] G. Ribert, D. Taieb, X. Petit, G. Lartigue, P. Domingo, Simulation of supercritical flows in rocket-motor engines: application to cooling channel and injection system, EUCASS Book Series 4 (2012) 205–226.
[29] K. Harstad, R. Miller, J. Bellan, Efficient high-pressure state equations, American Institute of Chemical Engineers Journal 43 (1997) 1605–1610.
[30] H. Meng, V. Yang, A unified treatment of general fluid thermodynamics and its application to a preconditioning scheme, Journal of Computational Physics 189 (2003) 277–304.
[31] M. Cismondi, J. Mollerup, Development and application of a three-parameter RK-PR equation of state, Fluid Phase Equilibria 232 (2005) 74–89.
[32] S.-K. Kim, H.-S. Choi, Y. Kim, Thermodynamic modeling based on a generalized cubic equation of state for kerosene/LOx rocket combustion, Combustion and Flame 159 (2012) 1351–1365.
[33] T. Chung, M. Ajlan, L. Lee, K. Starling, Generalized multiparameter corresponding state correlation for polyatomic, polar fluid transport properties, Industrial and Engineering Chemistry Research 27 (1988) 671–679.
[34] S. Takahashi, Preparation of a generalized chart for the diffusion coefficient of gases at high pressures, Journal of Chemical Engineering of Japan 7 (1974) 417.
[35] D. Lilly, A proposed modification of the germano sub-grid scale closure method, Physics of Fluids 3 (1991) 633–635.
[36] A. Vreman, An eddy-viscosity subgrid-scale model for turbulent shear flow: Algebraic theory and applications, Physics of Fluids 16 (2004) 3610–3681.
[37] F. Ducros, F. Laporte, T. Souleres, V. Guinot, P. Moinat, B. Caruelle, High-order fluxes for conservative skew-symmetric-like schemes in structured meshes: application to compressible flows, Journal of Computational Physics 161 (2000) 114–139.
[38] A. Jameson, W. Schmidt, E. Turkel, Numerical solution of the Euler equations by finite volume method using Runge-Kutta time stepping schemes, American Institute of Aeronautics and Astronautics, Paper 1259:1281 (1981).
[39] S. Tatsumi, L. Martinelli, A. Jameson, Flux-limited schemes for the compressible Navier–Stokes equations, American Institute of Aeronautics and Astronautics Journal 33 (2) (1995) 252–261.
[40] T. Poinsot, D. Veynante, Theoretical and Numerical Combustion., 3rd ed., 2012.
[41] N. Okong'o, J. Bellan, Consistent boundary conditions for multicomponent real gas mixtures based on characteristic waves, Journal of Computational Physics 176 (2002) 330–344.
[42] D. Taieb, G. Ribert, V. Yang, Supercritical fluid behavior in a cooling channel, in: American Institute of Aeronautics and Astronautics Paper, 49th Aerospace Sciences Meeting, 2011.
[43] T. Schmitt, L. Selle, A. Ruiz, B. Cuenot, Large-eddy simulation of supercritical-pressure round jets, American Institute of Aeronautics and Astronautics Journal 48 (9) (2010) 2133–2144.
[44] J. Bardina, J. Ferziger, W. Reynolds, Improved subgrid scale models for large eddy simulation, American Institute of Aeronautics and Astronautics Paper, 13th Fluid and Plasma Dynamics 1980-1357 (1980).
[45] J. Boris, F. Grinstein, E. Oran, R. Kolbe, New insights into Large Eddy Simulation, Fluid Dynamics Research 10 (1992) 199–227.

[46] M. Habiballah, L. Vingert, T.J.P. Vuillermoz, A test bench for cryogenic combustion research, 1996, in: 47th International Astronautical Congress, Beijing, China, 1996.
[47] O. Haidn, M. Habiballah, Research on high pressure cryogenic combustion, Aerospace Science and Technology 7 (2003) 473–491.
[48] M. Habiballah, M. Orain, F. Grisch, L. Vingert, P. Gicquel, Experimental studies on high-pressure cryogenic flames on the mascotte facility, Combustion Science and Technology 178 (2006) 101–128.
[49] T. Poinsot, S. Lele, Boundary conditions for direct simulations of compressible viscous flows, Journal of Computational Physics 101 (1987) 104–129.
[50] K. Thompson, Time dependent boundary conditions for hyperbolic systems, Journal of Computational Physics 68 (1987) 1–24.
[51] K. Thompson, Time dependent boundary conditions for hyperbolic systems, II, Journal of Computational Physics 89 (1990) 439–461.